photonics

MDPI

Article

Study on the Imaging Interference of a Vortex-Light-Modulated Gaussian Beam

Yanghe Liu [1], Yuanhe Tang [2,*], Jian Zhou [2], Cunxia Li [2], Ningju Hui [2], Yishan Zhang [2] and Yanlong Wang [2]

[1] School of Mechanical and Precision Instrument Engineering, Xi'an University of Technology, Xi'an 710048, China; 1220210023@stu.xaut.edu.cn
[2] School of Science, Xi'an University of Technology, Xi'an 710048, China; 13992517876@163.com (J.Z.); licunxia@xaut.edu.cn (C.L.); huiningju@xaut.edu.cn (N.H.); 2220920061@stu.xaut.edu.cn (Y.Z.); 2220920059@stu.xaut.edu.cn (Y.W.)
* Correspondence: ltp1801@163.com; Tel.: +86-029-82066357

Abstract: Combined with vortex light and airglow, some different physical phenomena are presented in this paper. Based on the ground-based airglow imaging interferometer (GBAII) made by our group, a liquid crystal on silicon (LCoS) device on one arm of a wide-angle Michelson interferometer (MI) of the GBAII is replaced by the reflector mirror to become the GBAII-LCoS system. LCoS generates a vortex phase to convert a Gaussian profile airglow into a vortex light pattern. After the Gaussian profile vortex light equation is obtained by combining the Gaussian profile airglow with the Laguerre–Gauss light, three different physical phenomena are obtained: the simulated Gaussian vortex airglow beam exhibits a hollow phenomenon with the introduction of the vortex phase, and as the topological charge (TC) l increases, the hollow range also increases; after adding the vortex factor, the interference fringe intensity can be 'broadened' with the optical path difference (OPD) and TC l increases, which match the field broadening technology for solid wide-angle MI; the 'Four-point algorithm' wind measurement for the upper atmosphere based on the vortex airglow is derived, which is different from the usual expressions. Some experimental results are presented: We obtained the influence modes of vortex light interference and a polarization angle from 335° to 245°. We also obtained a series of interference images that verifies the rotation of the vortex light, onto which is loaded a set of superimposed vortex phase images with TC l = 3 into LCoS in turn, and the interference image is rotated under the condition of the polarization angle of 245°. The controlled vortex interference image for different TC and grayscale values are completed.

Keywords: vortex light; LCoS; imaging interference; airglow

Citation: Liu, Y.; Tang, Y.; Zhou, J.; Li, C.; Hui, N.; Zhang, Y.; Wang, Y. Study on the Imaging Interference of a Vortex-Light-Modulated Gaussian Beam. *Photonics* **2024**, *11*, 557. https://doi.org/10.3390/photonics11060557

Received: 12 May 2024
Revised: 3 June 2024
Accepted: 7 June 2024
Published: 13 June 2024

1. Introduction

Vortex light has many unique properties: spiral wavefront, phase singularity, generation of dark hollow beams, etc. [1,2]. In 1979, Vaughan and Willetts studied the phase structure of vortex light. They studied the phase distribution of the ring-mode Laguerre–Gaussian beam (LGB) generated by the laser and found that such beams had phase singularity on the optical axis with zero intensity [3]. In 1996, the application of Laguerre–Gaussian vortex beams (LGVBs) in Doppler cooling was studied by Yoshio Tomura et al. [4]. In 2008, Moreno I et al. studied the effect of the optical device liquid crystal on silicon (LCoS) on the polarization state of the incident beam, and obtained the modulation results of the phase and amplitude of the incident light when LCoS applied different external voltages [5]. In 2012, Zhang Z C used the phase compensation to improve the spatial inhomogeneity of the phase-only LCoS spatial light modulator, which greatly reduced crosstalk and improved the diffraction rate of light [6]. In 2023, Kai Huang et al. studied a partially coherent LGVB and simulated the results of propagation in atmospheric turbulence [7]. There are many methods to generate vortex light, such as computational holography [8] and spatial light modulation [9]. In 2003, Jennifer E Curtis et al. used a liquid crystal spatial light modulator

(SLM) to generate a vortex beam, completed the capture of a colloidal polystyrene sphere, and discussed the radius of the vortex ring and the period of particle rotation [10]. In 2008, Naoya Matsumoto used LCoS to generate high-order LGVB and made a detailed analysis and discussion on how the mode of the incident light affects the outgoing LGVB. The results show that the top-hat incident beam can obtain a higher quality LGB [9]. In 2014, García-García, J et al. proposed a method for generating perfect vortex light, and the results were obtained using SLM [1]. In 2024, Ruediger Grunwald et al. used SLM to generate a vortex beam and extracted the parameters of a single or a group of distorted non-uniform vortex images by Fixed Circle Fourier Transform and Scanning Circle Fourier Transform [11].

Airglow is often used as a light source for the passive remote sensing to detect the upper atmospheric parameters of wind velocity, temperature, volume emissivity rate (VER), etc., such as the Earth [12] and Mars [13]. The emission spectral profile of common light sources includes Gaussian, Lorentz, and Voigt profiles. The Gaussian profile airglow in the middle and upper atmosphere is often used as the source of ground-based remote sensing wind measurements in middle and low latitudes. The vortex structure system widely exists in nature. When the plane light wave has similar characteristics to the 'spiral defect' in the crystal, the wavefront will rotate around the direction of propagation to form a spiral wavefront. An optical wave with such characteristics is called 'Optical Vortices' (OVs). When our GBAII (ground-based airglow imaging interferometer) was used to capture the Gaussian profile airglow of the O_2 (0–1) band of 865.2–867.9 nm with a peak altitude of 94 km and the O (^{1}S) band of 557.7 nm with a peak altitude of 98 km over the Earth, and obtained the atmospheric wind velocity, temperature, VER, number density, and other parameters [14,15] of 90–100 km above the Earth, some vortex light characteristics were found. In the present paper, we use a LCoS to replace a mirror of the MI (Michelson interferometer) arm in the GBAII [16] system to form a GBAII-LCoS interference system.

Although some of the aforementioned researchers have used liquid crystal SLM to generate a vortex beam and achieved considerable results, we note that there are no relevant experimental results on the issue of 'how polarization affects the shape of vortex interference images'. Because LCoS is added to the GBAII-LCoS system and a vortex beam is introduced, we need to consider the influence of polarization on interference imaging; so that there was the research origin study in this paper. In the process of our research, we thought about how to control the motion of the vortex light after interference and finally obtained some results.

In this paper, we study the combination of vortex light and Gaussian profile airglow to discover the special physical phenomenon from the imaging interference technology in GBAII-LCoS of a wide-angle Michelson interferometer (MI). The background of Gaussian profile airglow and vortex light is deduced in Section 1. In Section 2, there are three contents: the Gaussian profile vortex airglow based on LCoS is derived and the 'broadened' fringe with different TC values is simulated the interference intensity of airglow broadens with the optical path difference (OPD) due to the vortex factor, and the new expression of 'Four-point algorithm' wind measurements with the vortex factor into the interference fringes. Some experimental results are obtained of the vortex interference fringes changing with the angle of polarization, and the rotation of the interference image is completed by loading the superimposed vortex phase image in Section 3. The conclusions are presented in Section 4. Finally, the experimental results and possible applications are presented in the Section 5.

2. Methods and Simulation

2.1. Gaussian Profile Airglow Vortex Light Based on LCoS

In the GBAII-LCoS system, LCoS is not only to realize four stepped phases for the traditional 'Four-point algorithm (FPA)' or 'Four-intensity method' wind measurement, but also can be used to control the electrically birefringence effect to realize phase modulation on the optical signal, and realize wavefront transformation on the optical wave to obtain

the vortex light. The relationship between the liquid crystal molecular rotation angle φ of LCoS and the applied voltage V is shown as follows [17]:

$$\varphi = \frac{\pi}{2} - 2\arctan[\exp(\frac{V_c - V}{V_o})] \quad (1)$$

where V_c is the threshold voltage, V_o is the saturated voltage. When the applied voltage V exceeds V_c but less than V_o, the liquid crystal molecules rotate along the direction of the electric field; when V exceeds V_o, the liquid crystal molecules stop rotating. The rotation of liquid crystal molecules will change the OPD of the incident light, and then change the phase. The phase change is [18]:

$$\delta = 2\beta - \arctan\{\frac{\alpha\beta\sin\omega[1-\cos(2\sqrt{\alpha^2+\beta^2})] - \beta\sqrt{\alpha^2+\beta^2}\cos\omega\sin(2\sqrt{\alpha^2+\beta^2})}{[\alpha^2+\beta^2\cos(2\sqrt{\alpha^2+\beta^2})]\cos\omega}\} \quad (2)$$

where α is the twist angle of the liquid crystal molecule, which is the rotated angle of the outgoing light relative to the incident light, β is voltage-dependent [18]. The applied voltage and grayscale image of LCoS are mapped to each other. By using driver software to load different grayscale values on LCoS, the applied voltage V can be changed to achieve the purpose of phase modulation. Loading a hologram on LCoS to modulate the phase of the incident light can realize the phase modulation of the incident light wave [10]:

$$\varphi = l\theta - 2\pi\mathrm{int}(l\theta/2\pi) \quad (3)$$

where θ is the angle, l is the TC, which can be an integer or a fraction. When the phase of incident plane light wave is modulated by LCoS, the light field at the focal plane behind the lens is [10]:

$$\psi_l(r,\theta,0) = \pi A^2 J_l(x)\exp(il\theta)\sum_{n=0}^{\infty}\frac{(-1)^{n+l/2}(\xi)^{l+2n}}{(l/2+n+1)n!(n+l)!} \quad (4)$$

where A is the radius of the incident pupil of the system, J_l (x) is the first kind of Bessel function of order l. The relationship between bright ring with the closest distance to the center and the maximum intensity and the center point is [10]: $R_l = a\lambda f(1+l/l_0)/\pi A$, where a = 2.585, l_0 = 9.80 [10].

Between the moving upper atmospheric specie and the GBAII-LCoS's CCD detector, the emitted spectrum is broadened in the Gaussian profile:

$$g_D(\nu,\nu_0) = \sqrt{\frac{\ln 2}{\pi}}\frac{1}{\alpha_D}e^{-[\frac{\ln 2}{(\alpha_D)^2}(\nu-\nu_0)^2]} \quad (5)$$

where ν_0 is the center frequency (frequency of zero wind speed), $\alpha_D = \nu_0\sqrt{(2kT\ln 2/m)}/c$ is the full width at half maximum (FWHM), m and T are the mass of the atmospheric specie and the ambient atmospheric temperature, respectively, k and c are the Boltzmann constant and the light velocity in vacuum, respectively. The most common complex amplitude expression of Laguerre–Gauss vortex beams (LGVB) is:

$$E(r,\theta,z) = \frac{c_{lp}^{LG}}{w(z)}\left(\frac{\sqrt{2}r}{w(z)}\right)^{|l|}\exp\left(-\frac{r^2}{w^2(z)}\right)L_p^{|l|}\left(\frac{2r^2}{w^2(z)}\right)\exp\left(-ik\frac{r^2}{2R(z)}\right)\cdot\exp(-il\theta)\exp(-ikz)\exp(-i\psi(z)) \quad (6)$$

where $L_p^{|l|}$ is the Laguerre polynomial, c_{lp}^{LG} is a constant, and the beam waist radius is w_0. Then $z_R = \pi\omega_0^2/\lambda$ other parameters are: $\omega(z) = \omega_0\sqrt{1+(z/z_R)^2}$, $R(z) = z[1+(z_R/z)^2]$, $\psi(z) = (|l| + 2p + 1)\arctan(z/z_R)$, p and l are radial and TC, respectively, which together represent LGVB of different modes. The complex amplitude expression of the fundamental mode (p = 0) vortex beam in (6) is:

$$E(r,\theta,z) = \frac{c_{l0}}{w(z)}\left(\frac{\sqrt{2}r}{w(z)}\right)^{|l|}\exp(-\frac{r^2}{w^2(z)})\exp(2ik\frac{r^2}{4(z^2+z_R^2)} - \arctan(\frac{z}{z_R}))\exp(-il\theta) \quad (7)$$

In view of the fact that the factor $\exp(-il\theta)$ in Equation (7) has the characteristics of vortex light, we couple it with the Gaussian profile airglow in Equation (5) to obtain the expression of Gaussian profile vortex light:

$$E(v,v_0) = E_0\frac{2}{\alpha_D}\sqrt{\frac{\ln 2}{\pi}}\exp[-4\ln 2\frac{(v-v_0)^2}{\alpha_D^2}]\exp(-il\theta) \quad (8)$$

where E_0 is the largest amplitude. We use LCoS to generate vortex beam and modulate the 0-order LGVB to obtain the simulation results of vortex beam based on Gaussian profile airglow, as shown in Figure 1. The light field of the general Gauss profile is shown in Figure 1a, and the results of the Gauss profile vortex light are shown in Figure 1b,c. The simulated light was selected as 1 of the 12 of O_2(0–1) airglows [14], and the wavelength was 867.7 nm. There are some novel results: The hollowing degree of image intensity increases with the increase of TC of l, i.e., the extincted part at the center increases with the increase of l shown in Figure 1b. With the increase in l, the center downward depression becomes larger and larger shown in Figure 1c. From the vortex phase diagram of Figure 1d, it can be seen that the phase of the vortex beam is changed by $2\pi l$ during the propagation of the vortex beam around the axis, and the whole phase surface is spiral. The spiral phase surface increases with the growth of l, and more the phase changes.

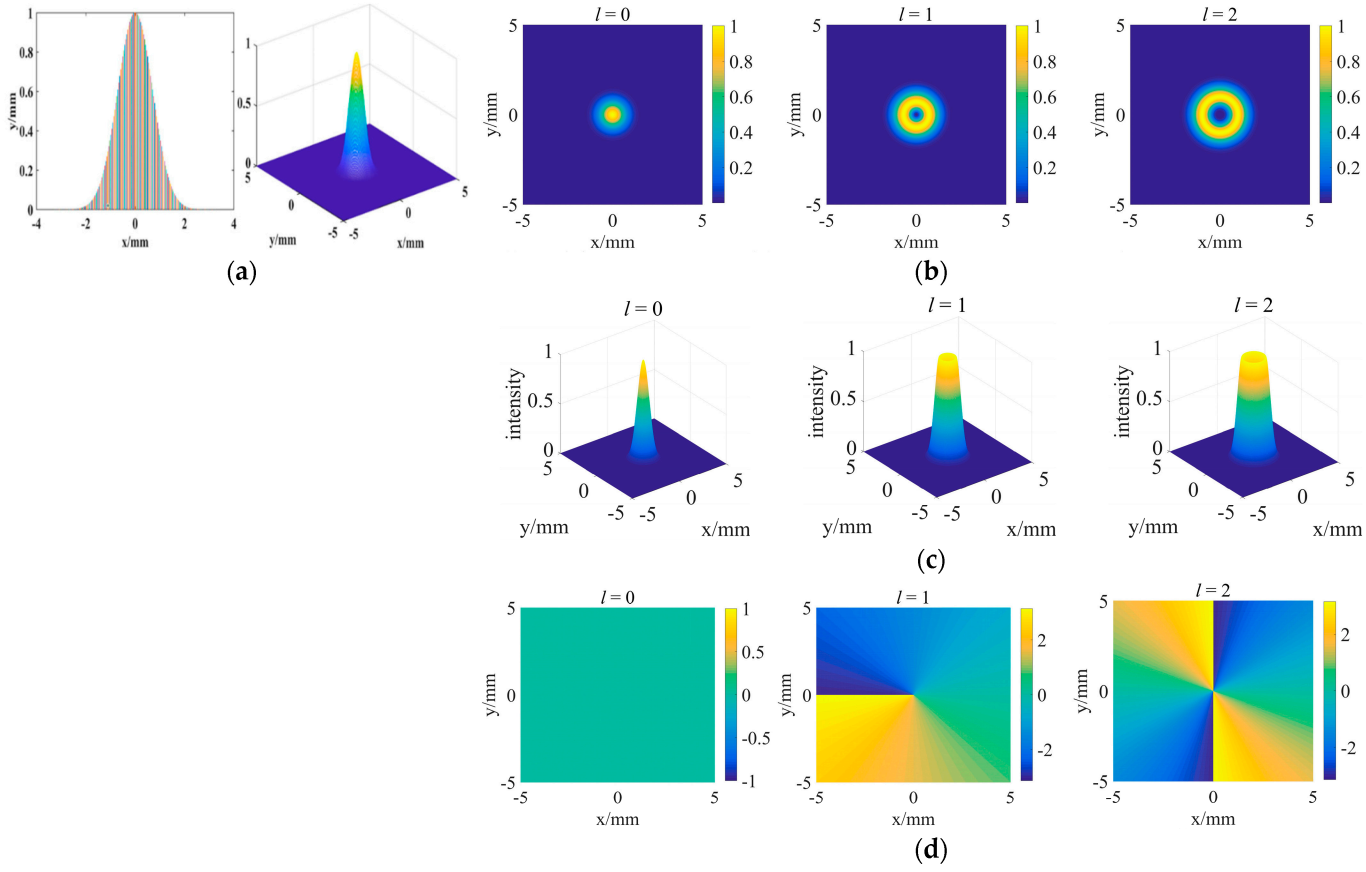

Figure 1. Modulation simulation results of Gaussian profile vortex beam: (**a**) simulation diagram of general Gaussian profile; (**b**) plane intensity diagram of Gauss vortex beam field with l = 0, 1, 2; (**c**) three-dimensional intensity diagram of Gaussian vortex beam field with l = 0, 1, 2; (**d**) plane phase diagram of Gaussian vortex beam with l = 0, 1, 2.

2.2. Interference Intensity of Airglow Broadens with the OPD Due to the Vortex Factor

A wide-angle MI with a large fixed OPD is necessary to realize the upper atmospheric wind passive measurement. For example, the fixed OPD of WINDII (Wind imaging interferometer) is 4.5 cm [12], and the fixed OPD of GBAII is 7.495 cm. Such a large OPD will theoretically produce 10^4–10^5 interference fringes, which is unfavorable to the experiment. In the actual wind measurement, the widen-angle MI broadening technology is used to compress the energy of the 10^4–10^5 fringes to 1–2 interference fringes [12,19,20], and then select one interference fringe to measure the wind velocity with the FPA [19]. Figure 2 is the GBAII-LCoS optical system, the widen-angle MI broadening and the imaging interferogram have been taken by GBAII-LCoS. The widen-angle MI broadening technique requires a strict coincidence of the MI two-arm mirror and the sub-beam of the LCoS. As shown in Figure 2c, Figure 2d is the imaging interferogram of the GBAII-LCoS with four different gray values obtained by the widen-angle MI broadening technique.

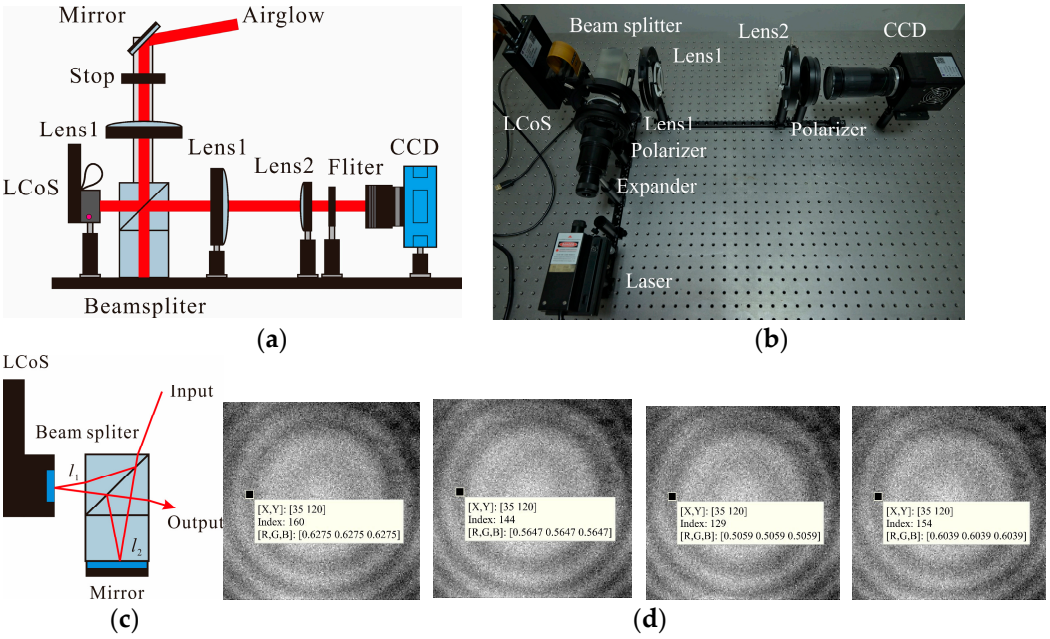

Figure 2. Wide-angle MI broadening of the GBAII-LCoS optical system and the resulting imaging interferograms: (**a**) GBAII-LCoS optical path diagram; (**b**) GBAII-LCoS physical chart; (**c**) solid schematic diagram of wide-angle MI field broadening; (**d**) imaging interferograms after broadening of GBAII-LCoS with gray value of 50, 100, 150, 200, from left to right.

It has been found that the spectral line can be broadened theoretically by introducing the vortex beam factor into the Gaussian profile airglow. After introducing the vortex phase, Gaussian profile airglow spectrum function [19] becomes:

$$B(\sigma) = B_0 \exp[-4\ln 2(\sigma - \sigma_0)^2/\omega^2] \exp(-il\theta) \tag{9}$$

where ω is the FWHM, σ is the wavenumber (σ_0 is the wavenumber at zero wind speed), and B_0 is the radiation max intensity. Through the MI interferometer, it is actually the effect of Fourier transform, and the interference intensity is:

$$I(\Delta) - \frac{1}{2}I(0) = B_0 \exp(i2\pi\sigma_0\Delta - l\theta) \int_{-\infty}^{+\infty} \exp(-4\ln 2\sigma^2/\omega^2) \exp(-i2\pi\sigma\Delta) \mathrm{d}\sigma \tag{10}$$

where Δ is OPD and $I(0)$ is the intensity at zero OPD. It is necessary to add the mirror symmetry of MI and simplification when considers the actual situation, and the relationship between the interference intensity and the OPD is further obtained:

$$I(\Delta) = I_0[1 + \exp(-QT\Delta^2)cos(2\pi\sigma_0\Delta - l\theta)] \tag{11}$$

where I_0 is the max intensity, $Q = 1.82\times10^{-12}(\sigma_0^2/M)(\mathrm{K}^{-1}\mathrm{cm}^{-2})$, M is the atomic mass, once the spectral profile is selected, Q is a constant, T is the atmospheric temperature at thermal equilibrium. After finishing, the Formula (11) is:

$$I(\Delta) = I_0[1 + V\cos(2\pi\sigma_0\Delta - l\theta)] \tag{12}$$

where V = exp $(-QT\Delta^2)$ is the visibility of fringe. By programming, we obtained the broadening results of Gaussian profile airglow with different TC l as shown in Figure 3, that is the interference intensity with l = 0,1,2. From these images, it can be observed that when the TC l is added, the shape of the curve changes and widens with the increase of l.

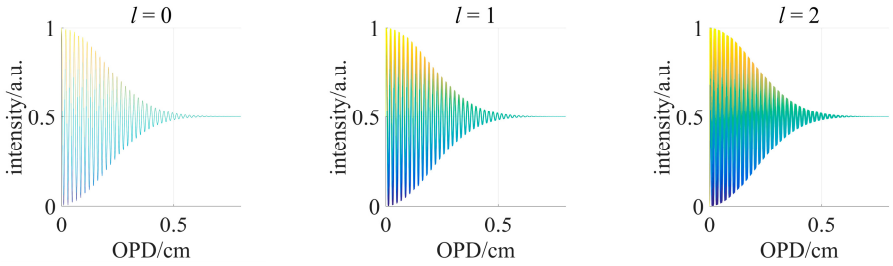

Figure 3. Intensity broadening results of Gaussian profile airglow with different TC of l.

After introducing the vortex beam into the upper atmospheric wind measurement, this 'broadening' effect will directly affect the results of inversion of subsequent wind velocity and the temperature measurement. It can be seen from Figure 3 that the vortex phase directly leads to the broadening of the OPD interval corresponding to the same intensity of interference, which reduces the sensitivity of the interference intensity to the OPD, that is, the uncertainty of the OPD within a certain range will not have an essential impact on the experimental results. That is also the application of the broadening of the interference fringes directly in wind measurement after the introduction of vortex factor. Organize Equation (12) to get:

$$\frac{I(\Delta) - I_0}{I_0} = \exp(-QT\Delta^2)\mathrm{Re}[\exp(il\theta)\exp(-i2\pi\sigma_0\Delta)] \tag{13}$$

Let $I = \ln[(I(\Delta) - I_0)/I_0)]$, after mathematical transformation, the relationship between interference intensity and OPD of Δ, l is shown as follows:

$$I = -QT\Delta^2 + \mathrm{Re}\sum_{n=0} i^{l-n}\cdot\frac{l(l-1)\ldots(l-n+1)}{n!}\cos^n(\theta)\sin^{l-n}(\theta) \tag{14}$$

where i is an imaginary unit. It can be seen from Equation (14) that when the interference intensity is constant, the OPD Δ fluctuates within a certain range, and the fluctuation can be balanced by the change of the vortex phase, which is the reason why the interference intensity shows 'broadening' on the OPD Δ. It can be observed from Figure 4 that the 'broadening' effect brought by different l is indeed different.

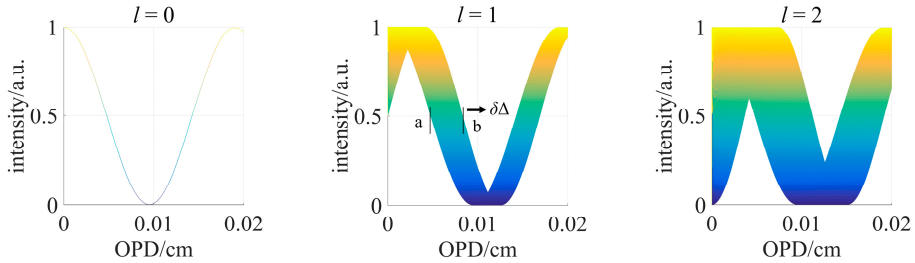

Figure 4. Broadening effect of the interference intensity corresponding to different TC of *l*.

After adding the vortex factor, we give the magnitude of the interference intensity broadening with the OPD. As shown in Figure 4, two points *a* and *b* with the same interference intensity *I*(a) are taken, because these two points are symmetrical about (*b* + *a*)/2. Assuming that the total length of the interval is *x* and divided into *n* parts, the total broadening length *H* of the *a* and *b* intervals with the same interference intensity is:

$$\mathrm{H} = (\mathrm{b} - \mathrm{a})\frac{x}{n} = \delta\Delta\frac{x}{n} \tag{15}$$

where $\delta\Delta$ is the OPD in the *a*-*b* interval, the wave number contained in the broadening stripe is N = int (H/λ), and λ is the airglow wavelength. After the vortex beam is introduced into the upper atmospheric wind measurement, the 'broadening' effect in theory will directly affect the inversion results of subsequent wind velocity and temperature measurement. The simulated vortex phase directly led to the broadening of the OPD interval corresponding to the same interference intensity as shown in Figure 4, the sensitivity of the interference intensity to the OPD is reduced, that is, the uncertainty of the OPD within a certain range will not have an essential impact on the experimental results. This is also the application of the broadening of the interference fringes directly in the wind measurement after the introduction of vortex beam factor, which theoretically makes up for the technical field broadening of the wind measurement wide-angle MI. As shown in Figure 2c, the physical field broadening can increase the observing field of the instrument and enhance the light collecting ability of the wide-angle MI.

2.3. New FPA Wind Measurement Based on Vortex Airglow

Due to the relative speed of v between the atmospheric specie and the GBAII's CCD detector along the line-of-sight (LOS), the Doppler effect causes the wave number σ to change to $\sigma = \sigma_0\,(1 + v/\mathrm{c})$ (σ_0 is zero wind wave number, $\sigma_0 = 1/\lambda_0$). The wind-angle MI for wind measurement need a large OPD Δ, for example, Δ = 7.495 cm for GBAII. The Δ is divided into a fixed OPD Δ_0 and a stepped OPD Δ': $\Delta = \Delta_0 + \Delta'$ ($\Delta_0 >> \Delta'$). We substituted it into Equation (12) and expanded it to obtain:

$$I(\Delta) = I_0[1 + V\cos(l\theta - \phi_0 + \phi_s + \phi_v)] \tag{16}$$

Let the OPD Δ' step 4 times: $\Delta' = 0, \lambda_0/4, 2\lambda_0/4, 3\lambda_0/4$, that is to say, the four stepped phases $\varphi_s = 0, \pi/2, \pi, 3\pi/2$ can be obtained. Substituting φ_s into Equation (16), The four intensities can be obtained:

$$\begin{aligned} I_1 &= I_0[1 + V\cos(l\theta - \phi_0 + \phi_v)] \\ I_2 &= I_0[1 - V\sin(l\theta - \phi_0 + \phi_v)] \\ I_3 &= I_0[1 - V\cos(l\theta - \phi_0 + \phi_v)] \\ I_4 &= I_0[1 + V\sin(l\theta - \phi_0 + \phi_v)] \end{aligned} \tag{17}$$

After calculating the expression of (17), the phase containing the wind speed of LOS can be obtained, and then the wind speed can be inversed:

$$v = \frac{c\phi_v}{2\pi\sigma_0\Delta_0} = \frac{c\arctan(\frac{I_4-I_2}{I_3-I_1})}{2\pi\sigma_0\Delta_0} \quad (18)$$

Equation (18) is to consider the new FPA wind measurement expression with TC l in Equation (17). By changing the Equation (16) step phase φ_s and TC l, the atmospheric wind speed in the LOS direction can be obtained by Equation (18). Rotating the pointing mirror at the front end of GBAII, and then get another vertical wind speed of LOS, so that the combined two-dimensional wind velocity can be obtained finally.

Based on the GBAII-LCoS experimental system shown in Figure 2b and the normal FPA, we originally wanted to use the image superimposed function of LCoS to superimpose the ordinary grayscale image with the vortex phase image, which realizes stepping and vortex modulation at the same time. However, when the superposition is completed, the rotated phenomenon of vortex phase diagram is found. The flow chart is shown in Figure 5a. The bit depth of LCoS is 8-bit (256 gray scale values). The 256 grayscale images are superimposed with any l vortex phase images to obtain a set of superimposed holograms. Figure 5b is the superimposed vortex phase diagram with l = 3, from which nine images are selected. It can be observed that when superimposed on the 255th grayscale image, the phase diagram rotates by one-third in the clockwise direction. The group of images is made into video (see Supplementary Materials for Video S0), and the image rotates by 2π phase. If the superimposed images (l = 3) are loaded into LCoS in sequence, the interference results will rotate in theory. The following is verified by experiments.

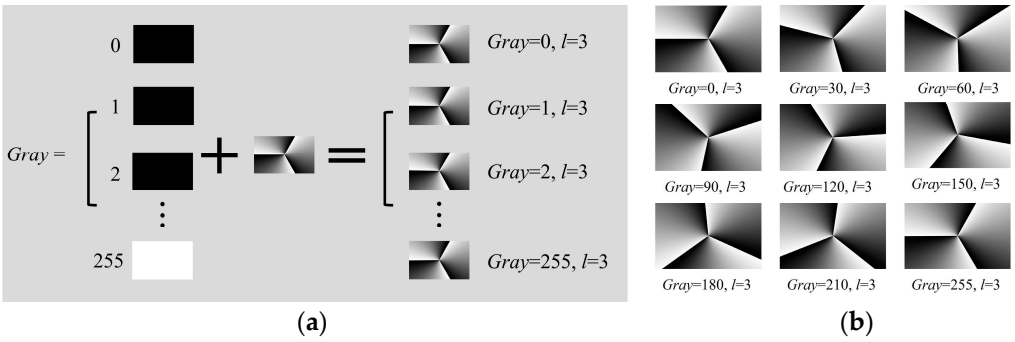

Figure 5. Superposition results of phase stepped grayscale image and vortex phase image of modulated LCoS in GBAII-LCoS: (**a**) flow chart of superposition of grayscale image and vortex phase image (l = 3); (**b**) superimposed result diagram.

3. Experimental Results of Gaussian Profile Vortex Imaging Interference Based on LCoS

In the second section, we derived and simulated the Gaussian profile vortex beam, and then we need to observe it through next experiments. Airglow is often used as a source for passive sensing of the upper atmospheric winds. Such as WINDII [12], Waves Michelson Interferometer (WAMI) [21], GBAII [14,15] and other passive sensing instruments all use the different airglow wavelength. In previous research, GBAII also used the Gaussian profile airglow to observe the atmospheric wind, temperature, etc., parameters at the altitude of 90–100 km atmosphere. Airglow is so weak that a long exposure time is required to collect it (GBAII uses a 3 min exposure time). At present, we initially combined the Gaussian profile airglow with a vortex beam. In the process of experiment, we may encounter some unknown problems. In order to find and solve problems in time, the use of laser is a better choice. Therefore, we temporarily chose a Gaussian laser with a wavelength of 532 nm to simulate the airglow as much as possible, and get the following experiments.

Experiment 1: Observing the results influencing of vortex light interference and polarization angle. The filter of GBAII-LCoS optical path in Figure 2a is removed. The

simplified optical path system is shown in Figure 6a. The imaging interference experiment of vortex light in the laboratory is carried out. Laser is divided into two beams after expanding into the beam splitter (BS). The two beams pass through the mirrors at the bottom of LCoS and BS respectively, and finally interfere with imaging in the camera CCD. The interference results are shown in Figure 6b–d. When the polarization angle η changes, we observe that the interference image has changed in different forms. Taking the interference results with l of 3, 10, and 20 as examples, when the polarized angle $\eta = 335°$, the interference image is a normal interference fringe. Next, the polarizer is rotated, and then the image begins to distort and the interference fringe begins to disappear during the rotation. When $\eta = 264°$, the normal interference fringe is almost invisible, shown in Figure 6b–d.

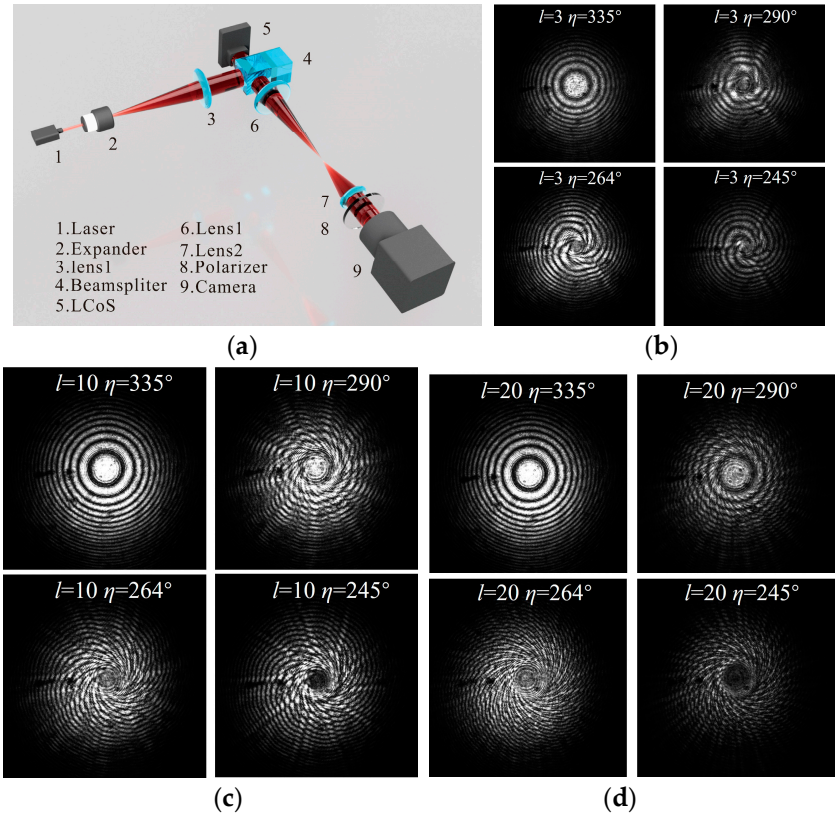

Figure 6. LCoS is modulated to obtain the imaging interferograms of different TC l vortex beams for the wide-angle MI arm of the GBAII-LCoS system: (**a**) Wide-angle MI optical path diagram of GBAII-LCoS; (**b**) vortex light imaging interferogram at $l = 3$, $\eta = 335°$, 290°, 264°, 245°; (**c**) vortex imaging interferograms at $l = 10$, $\eta = 335°$, 290°, 264°, 245°; (**d**) vortex imaging interferograms at $l = 20$, $\eta = 335°$, 290°, 264°, 245°.

The reasons for the influence of interference morphology are as follows: (1) Polarization: Experiments have proved that polarization has an effect on the interference results. It may be that the polarization direction of the incident beam has an angle with the fast and slow axes of the liquid crystal molecules, which makes the profile of the interference image between the circular fringes and the vortex fringes. After changing the polarization direction through the polarizer, the profile of the imaging appears as circular fringes and vortex fringes. The deeper reason is that we are exploring; (2) Unmodulated reflected beam: The liquid crystal target surface of LCoS is composed of a number of pixels, and there are some gaps between the pixels. These unfilled gaps will not modulate the incident beam, but will be reflected with the modulated incident beam. The two are doped together to affect the final interference result.

Experiment 2: Verifying the rotation of the vortex light interference image. Under the condition of polarization angle $\eta = 245°$, we loaded a set of $l = 3$ superimposed vortex phase diagrams, and obtained the experimental results of rotational interferometry, as shown in Figure 7, and the images with gray levels of 0, 30, 60, 90, 120, 150, 180, 210, and 255 are selected It can be observed that the interference image has rotated. Video result Video S1 is shown in the Supplementary Material. This result is consistent with the results of Figure 5b, and the corresponding theory is verified by the experiments.

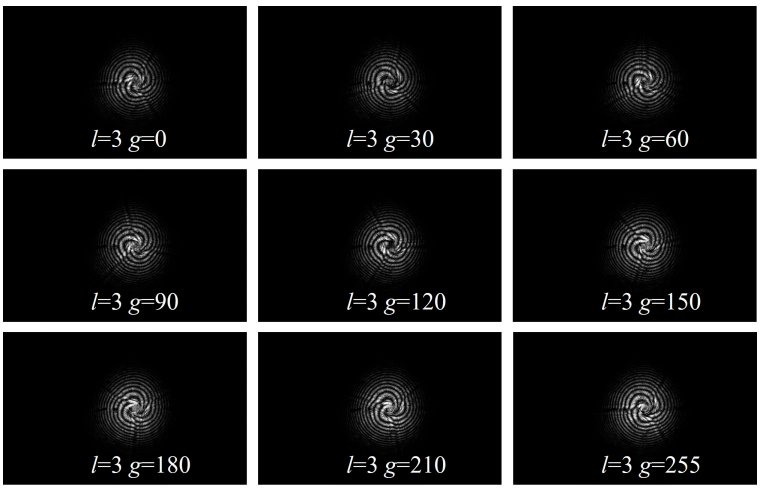

Figure 7. Imaging interferograms with different gray corresponding to the rotation of TC $l = 3$.

4. Conclusions

In this paper, the following conclusions are drawn through Gaussian profile vortex light theory, simulation, and experiment: (1) Gaussian profile airglow is combined with LGVB to obtain and simulate Gaussian profile vortex light. The phenomenon of beam hollowing is observed, and the hollow range increases with the increase of TC l. In the process of simulating interference, it is observed that the interference fringes have a certain 'broadening' phenomenon, and the width of 'broadening' also gradually widens with the increase of TC l. (2) Using the image superimposed function of LCoS to superimpose the 8-bit grayscale image with the vortex phase image, the superimposed image can rotate in a clockwise direction. (3) We used the GBAII-LCoS system to obtain the interference phenomenon of vortex beam with TC $l = 3$, and the influence of polarization on vortex interference was observed at the same time. When the polarizer is rotated from 335° to 264°, the interference image gradually changes from the ring to the vortex, and then to 245°, the image changes to the ring shape. (4) After a set of superimposed vortex phase images with $l = 3$ (256) are loaded into LCoS in turn, the interference image is rotated also. The rotated control of the interference vortex beam is completed by this image superposition method, and the speed of rotation can be controlled by the loading speed.

5. Discussion

Compared with some of the research in the literature mentioned above, we observed the effect of polarization on the interference imaging of vortex beam. Because the liquid crystal molecule is one of the core components of LCoS, the polarized direction of the incident beam will affect the experimental results. From the experimental results of Figure 6, the polarization has an effect on the profile of the imaging interference. The angle between the polarized direction of the incident beam and the liquid crystal molecule may be one of the influencing factors. Because the liquid crystal molecule of LCoS also has a certain angle under the influence of voltage, the incident light beam that does not change the direction of polarization may have an angle with the long axis or slow axis of the liquid crystal molecule, so the profile of the imaging interference is between the circular fringe

and the vortex fringe. In the process of rotating the polarizer, the polarization direction of the incident beam changes continuously, making the circular fringes and vortex fringes appear again. Since the research group has initially introduced the vortex beam, we are also analyzing the deeper reasons. In addition, there are unfilled gaps between the pixels of liquid crystal target surface of LCoS. These gaps will reflect a part of the unmodulated incident beam and affect the results of interference. In subsequent research, we need to separate these unmodulated beams. At present, our experiment focuses more on the observation of vortex interference phenomenon, and the vortex imaging remains to be studied. From the experimental results, the imaging and interference quality are reduced after introducing the vortex beam. The imaging quality is to be described according to the modulation transfer function (MTF). We will continue to improve the MTF on the CCD imaging focal plane after adding the vortex factor, so that the instrument can obtain clearer imaging interference results with obvious vortex characteristics.

In this paper, a Gaussian profile laser is used instead of airglow in the experiment. This is because the intensity of airglow is so weak, and it takes a long exposure time to collect outdoors, while the laser is relatively more efficient. Therefore, we use Gaussian laser to simulate Gaussian profile airglow as much as possible, observe more phenomena in the laboratory, and find shortcomings and deficiencies so that we can improve it in time. Although the experimental results and experience of Gaussian laser are not fully applicable to Gaussian profile airglow, as a Gaussian light source, the experimental results of laser can also provide reference and analogy method for outdoor airglow vortex beam experiment, which is the connection between these two sources. In the follow-up study, we will gradually improve the interference experiment of airglow vortex beam outdoors.

The vortex beam control results in Figure 7 remind us of the application of particle manipulation. The vortex beam itself has orbital angular momentum (OAM), which can make the particles rotate, and the rotated velocity can be controlled by the number of TC l. If we let the vortex beam itself rotate, can we accelerate or decelerate the rotation of the particles without changing the TC l? This is also a new problem extended in this paper. In addition to the phenomenon in Figure 7, we have some interesting ideas for Gaussian vortex beam, such as communication, coding, etc., which we will actively explore in the future.

Supplementary Materials: The following supporting information can be downloaded at: https://www.mdpi.com/article/10.3390/photonics11060557/s1, Video S0: Rotation of vortex phase diagram (l = 3), Video S1: Rotation of interference image (l = 3).

Author Contributions: Conceptualization, Y.T., Y.L. and J.Z.; methodology, Y.L. and J.Z.; software, Y.L. and J.Z.; validation, Y.L., J.Z. and Y.W.; formal analysis, J.Z., C.L. and N.H.; investigation, Y.Z. and Y.W. All authors have read and agreed to the published version of the manuscript.

Funding: This work was funded by the National Natural Science Foundation of China (41975040), Shaanxi Natural Science Foundation (2020JZ-46, 2021JQ-469) and Youth Innovation Team Project of Shaanxi Education Department (23JP118).

Institutional Review Board Statement: Not applicable.

Informed Consent Statement: Not applicable.

Data Availability Statement: Data are contained within the article.

Conflicts of Interest: The authors declare no conflicts of interest.

References

1. García-García, J.; Rickenstorff-Parrao, C.; Ramos-García, R.; Arrizón, V.; Ostrovsky, A.S. Simple Technique for Generating the Perfect Optical Vortex. *Opt. Lett.* **2014**, *39*, 5305–5308. [CrossRef] [PubMed]
2. Zhou, X.; Zhu, Z.; Xie, X.; Yao, L.; Fan, F.; Zhou, Y. Broadband Vortex Beam Modulating System Based on Electrically Controlled Liquid Crystal Devices. *Photonics* **2023**, *10*, 1012. [CrossRef]
3. Vaughan, J.M.; Willetts, D.V. Interference Properties of a Light Beam Having a Helical Wave Surface. *Opt. Commun.* **1979**, *30*, 263–267. [CrossRef]

4. Kuga, T.; Torii, Y.; Shiokawa, N.; Hirano, T.; Shimizu, Y.; Sasada, H. Novel Optical Trap of Atoms with a Doughnut Beam. *Phys. Rev. Lett.* **1997**, *78*, 4713–4716. [CrossRef]
5. Moreno, I.; Lizana, A.; Campos, J.; Márquez, A.; Iemmi, C.; Yzuel, M.J. Combined Mueller and Jones Matrix Method for the Evaluation of the Complex Modulation in a Liquid-Crystal-on-Silicon Display. *Opt. Lett.* **2008**, *33*, 627–629. [CrossRef] [PubMed]
6. Zhang, Z.; Yang, H.; Robertson, B.; Redmond, M.; Pivnenko, M.; Collings, N.; Crossland, W.A.; Chu, D. Diffraction Based Phase Compensation Method for Phase-Only Liquid Crystal on Silicon Devices in Operation. *Appl. Opt.* **2012**, *51*, 3837–3846. [CrossRef] [PubMed]
7. Huang, K.; Xu, Y.; Li, Y. Average Intensity of a Laguerre—Gaussian Vector Vortex Beam through Inhomogeneous Atmospheric Turbulence. *Photonics* **2023**, *10*, 1189. [CrossRef]
8. Heckenberg, N.R.; McDuff, R.; Smith, C.P.; White, A.G. Generation of Optical Phase Singularities by Computer-Generated Holograms. *Opt. Lett.* **1992**, *17*, 221–223. [CrossRef] [PubMed]
9. Matsumoto, N.; Ando, T.; Inoue, T.; Ohtake, Y.; Fukuchi, N.; Hara, T. Generation of High-Quality Higher-Order Laguerre-Gaussian Beams Using Liquid-Crystal-on-Silicon Spatial Light Modulators. *J. Opt. Soc. Am. A* **2008**, *25*, 1642–1651. [CrossRef]
10. Curtis, J.E.; Grier, D.G. Structure of Optical Vortices. *Phys. Rev. Lett.* **2003**, *90*, 133901-1–133901-4. [CrossRef] [PubMed]
11. Grunwald, R.; Bock, M. Characterization of Orbital Angular Momentum Beams by Polar Mapping and Fourier Transform. *Photonics* **2024**, *11*, 296. [CrossRef]
12. Shepherd, G.G.; Thuillier, G.; Gault, W.A.; Solheim, B.H.; Hersom, C.; Alunni, J.M.; Brun, J.-F.; Brune, S.; Charlot, P.; Cogger, L.L.; et al. WINDII, the Wind Imaging Interferometer on the Upper Atmosphere Research Satellite. *J. Geophys. Res.* **1993**, *98*, 10725–10750. [CrossRef]
13. Rong, P.; Zhang, C.; Ward, W.E.; Zhu, H.; Dai, H. Compensation Optimization for a Static Mars Wind Imaging Michelson Interferometer. *Opt. Lasers Eng.* **2021**, *142*, 106589. [CrossRef]
14. Gao, H.; Tang, Y.; Hua, D.; Liu, H.; Cao, X.; Duan, X.; Jia, Q.; Qu, O.; Wu, Y. Ground-Based Airglow Imaging Interferometer Part 1: Instrument and Observation. *Appl. Opt.* **2013**, *52*, 8650–8660. [CrossRef] [PubMed]
15. Tang, Y.; Duan, X.; Gao, H.; Qu, O.; Jia, Q.; Cao, X.; Wei, S.; Yang, R. Ground-Based Airglow Imaging Interferometer Part 2: Forward Model and Inverse Method. *Appl. Opt.* **2014**, *53*, 2273–2282. [CrossRef] [PubMed]
16. Gao, H.; Hua, D.; Tang, Y.; Cao, X.; Liu, H.; Jia, W. Wide-Angle Michelson Interferometer Based on LCoS. *Opt. Commun.* **2013**, *292*, 36–41. [CrossRef]
17. Lu, Q.; Sheng, L.; Zhang, X.; Bai, J.; Qiao, Y. Investigation on Pure Phase Modulation Characteristics of Liquid Crystal Spatial Light Modulator at Oblique Incidence. *Chin. J. Laser* **2016**, *43*, 0112001-1–0112001-7. [CrossRef]
18. Ge, A.M.; Sui, Z.; Xu, K.S. Characteristics of phase-only modulation using a reflective liquid crystal on silicon device. *Chin. J. Phys.* **2003**, *52*, 2481–2485.
19. Hilliard, R.L.; Shepherd, G.G. Wide-Angle Michelson Interferometer for Measuring Doppler Line Widths*. *J. Opt. Soc. Am.* **1966**, *56*, 362–369. [CrossRef]
20. Gault, W.A.; Shepherd, G.G. WAMDII—A Wide Angle Michelson Doppler Imaging Interferometer for Spacelab. *Adv. Space Res.* **1982**, *2*, 111–114. [CrossRef]
21. Ward, W.E.; Gault, W.A.; Shepherd, G.G.; Rowlands, N. *Waves Michelson Interferometer: A Visible/Near-IR Interferometer for Observing Middle Atmosphere Dynamics and Constituents*; Fujisada, H., Lurie, J.B., Weber, K., Eds.; SPIE: Toulouse, France, 2001; pp. 100–111. [CrossRef]